



**HAL**  
open science

# Neutral, charged excitons and biexcitons in strain-free and asymmetric GaAs quantum dots fabricated by local droplet etching

Z. Trabelsi, M. Yahyaoui, S. Ben Radhia, K. Boujdaria, E. Zallo, O.G. Schmidt, P. Atkinson, M. Chamarro, C. Testelin

## ► To cite this version:

Z. Trabelsi, M. Yahyaoui, S. Ben Radhia, K. Boujdaria, E. Zallo, et al.. Neutral, charged excitons and biexcitons in strain-free and asymmetric GaAs quantum dots fabricated by local droplet etching. *Journal of Luminescence*, 2018, 197, pp.47-55. 10.1016/j.jlumin.2018.01.012 . hal-02390097

**HAL Id: hal-02390097**

**<https://hal.science/hal-02390097>**

Submitted on 20 Apr 2023

**HAL** is a multi-disciplinary open access archive for the deposit and dissemination of scientific research documents, whether they are published or not. The documents may come from teaching and research institutions in France or abroad, or from public or private research centers.

L'archive ouverte pluridisciplinaire **HAL**, est destinée au dépôt et à la diffusion de documents scientifiques de niveau recherche, publiés ou non, émanant des établissements d'enseignement et de recherche français ou étrangers, des laboratoires publics ou privés.

# Neutral, charged excitons and biexcitons in strain-free and asymmetric GaAs quantum dots fabricated by local droplet etching

Z. Trabelsi<sup>1</sup>, M. Yahyaoui<sup>1</sup>, S. Ben Radhia<sup>1</sup>, K. Boujdaria<sup>1</sup>, E. Zallo<sup>2,3</sup>,  
O. G. Schmidt<sup>2</sup>, <sup>4</sup>P. Atkinson, <sup>4</sup>M. Chamarro, and <sup>4</sup>C. Testelin

<sup>1</sup>*Laboratoire de Physique des Matériaux: Structure et Propriétés,  
Faculté des Sciences de Bizerte, Université de Carthage, 7021 Zarzouna, Bizerte, Tunisia*

<sup>2</sup>*Institute for Integrative Nanosciences, IFW Dresden,  
Helmholtzstrasse 20, 01069 Dresden, Germany*

<sup>3</sup>*Paul-Drude-Institut für Festkörperelektronik,  
Hausvogteiplatz 5-7, D-10117, Berlin, Germany and*

<sup>4</sup>*Sorbonne Universités, UPMC Univ Paris 06, CNRS-UMR 7588,  
Institut des NanoSciences de Paris, F-75005, Paris, France*

(Dated: December 23, 2017)

## Abstract

We present an experimental and theoretical study of the optical properties of asymmetric strain-free GaAs quantum dots (QDs) fabricated by filling of self-organized nanoholes (NHs) created by local droplet etching. The energy levels are calculated within the effective mass approximation using as input a model anisotropic QD shape with  $C_{2v}$  symmetry based on atomic force microscopy (AFM) profiles of NHs. The influence of the QD height and shape anisotropy on the exciton emission energy and the  $s$ - $p_x$  and  $s$ - $p_y$  energy splittings is studied theoretically. The experimentally observed bound nature of excitonic states is well reproduced by our theoretical approach which includes direct Coulomb energies and correlation effects. We investigate the fine-structure splitting (FSS) of the neutral exciton as a function of dot size. Theoretical calculations of the long-range electron-hole (e-h) exchange interaction predict an increase of the FSS with decreasing QD height, which describes well the experimental trend.

PACS numbers: 73.21.La, 68.65.Hb

## 1. Introduction

Strain-free GaAs/AlGaAs quantum dots (QDs) are a relatively new III-V QD family of great interest. One method to grow these dots is droplet epitaxy, and highly symmetric, high optical quality strain-free dots have been fabricated on (111) substrates by this technique [1–3]. An alternative QD growth method is self-assembled local droplet etching (LDE) and nanohole infilling [4–7]. This technique is particularly attractive since the dot density and emission energy can be controlled independently with the QD size precisely controlled via the hole filling level [7, 8]; both anisotropic and highly symmetric dots can be grown by suitable choice of droplet etching conditions [9, 10]; and quantum dot molecules can be realized and implemented in devices [11]. This makes these strain-free GaAs/AlGaAs QDs potentially useful for applications such as QD lasers [12] and solar cells [13]. However, for the realization of QD based devices, the dependence of the QD optical properties, namely, the exciton transition energies and intersublevel energy spacing on the QD shape and size needs to be well understood.

The asymmetry of QDs is of particular interest also for quantum information applications since symmetric dots are attractive due to the low value of exciton fine-structure splitting (FSS), which makes them promising systems for entangled photon sources, while highly asymmetric dots have the potential to lead to brightening of the long-lived dark exciton state, which is of interest for spin-based quantum processing [14]. Since GaAs/AlGaAs QDs are nominally unstrained and have sharp interfaces with little intermixing, they provide an ideal system to study the role of the geometric anisotropy in determining QD electronic properties, such as the FSS.

Recently, a few studies [5–7] have focused on the optoelectronic properties of strain-free GaAs QDs, however theoretical investigations are still required. In our recent work [15], we presented a theoretical study of the optical transitions of different excitonic complexes in highly symmetric strain-free GaAs quantum dots (QDs) fabricated by epitaxially filling nanoholes (NHs) in AlGaAs surface. The QD energy levels were calculated using a model of the QD shape and size based on atomic force microscopy (AFM) measurements of the QD, and the calculated levels showed reasonable agreement with photoluminescence measurements demonstrating the suitability of our modelling approach. Nevertheless, the majority of the QDs fabricated by local droplet etching technique are slightly anisotropic [8, 16–18].

Hence, taking into account such anisotropy in our modelling approach is necessary. Here, we give a comprehensive outline of our theoretical approach which is supported by a good agreement with optical spectroscopic study, performed on GaAs QDs. Since we are interested in asymmetric QDs, we investigate the exciton FSS, due to the electron-hole (e-h) exchange interaction, as a function of the QD height.

The paper is organized as follows. Section **2** is divided into two parts. In part **2.1.**, we present micro-photoluminescence ( $\mu$ -PL) measurements of single GaAs QDs obtained by filling NHs with different amounts of GaAs. In part **2.2.**, we outline our theoretical model which includes the QD shape modelling and the calculation of the confined states. The numerical results are presented in section **3** where we perform a comparison between experimental data and theoretical results, and we study the few-particle binding energies and correlation effects. Exchange interaction effects and exciton FSS will also be evaluated and discussed. Our results are summarized in section **4**.

## 2. Methods

### 2.1. Samples and experimental setup

The samples have been grown by solid source molecular beam epitaxy on GaAs (100) substrate. Details of the gallium droplet etching process used to form the nanohole can be found in Ref. [7]. The nanoholes were then overgrown by a 7 nm  $\text{Al}_{0.45}\text{Ga}_{0.55}\text{As}$  barrier, a GaAs layer with nominal thickness from 0.25 to 3.5 nm, and an upper  $\text{Al}_{0.33}\text{Ga}_{0.67}\text{As}$  barrier. A 2 minute growth interruption ensured significant GaAs migration towards the bottom of the NH such that the GaAs thickness at the bottom is significantly larger than the nominal deposited thickness.

Figure 1 shows the shape of the NH after growth of the lower AlGaAs barrier (left image, black lines) and after growth of a subsequent 1 nm GaAs layer followed by 2 minute growth interruption (right image, blue lines). It can be seen that the NHs, which have a typical depth of 8 nm before growth of the GaAs layer, are elongated along the [110] direction, with an in-plane anisotropy (ratio of the width along [110] to the width along  $[\bar{1}10]$ ) given by  $\beta \approx 2.5$ . It can be seen that net migration towards the bottom of the hole results in a dot, approximately 4 nm high, confined in the NH for a nominally 1 nm deposition.

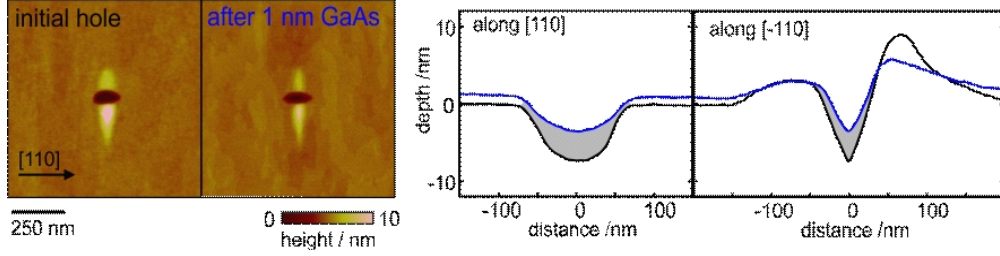


Fig. 1: AFM images of an *in-situ* etched nanohole where the growth was stopped after: overgrowth of 7 nm  $\text{Al}_{0.45}\text{Ga}_{0.55}\text{As}$  bottom barrier layer (left image), overgrowth of the bottom AlGaAs barrier layer and 1 nm GaAs layer followed by a 2 minute growth interruption (right image). Corresponding surface profiles along the  $[110]$  and  $[\bar{1}10]$  directions, which are the average from ten measured nanoholes, are shown for the bottom barrier layer (black line) and top of the GaAs layer (blue line). The gray shaded area indicates the location and form of the QD.

$\mu$ -PL measurements were carried out at 10 K using a 532 nm Nd:YVO4 excitation laser focused down to  $\approx 1\mu\text{m}^2$  and a spectrometer with  $\approx 40\mu\text{eV}$  resolution. The dot density was low enough to enable single dot spectroscopy to be carried out without any need for sample processing.

The  $\mu$ -PL polarization was analyzed by including a half-wave plate and a linear polarizer before detection. The fine structure splitting of the exciton can then be observed (see Inset Fig. 2(b)).

$\mu$ -PL spectra obtained for different nominal thicknesses are shown on Fig. 2. For each sample, one detects a strong emission peak associated to the neutral exciton of a single QD, labelled  $X$ , (more precisely, an electron-hole pair in a neutral QD), determined by polarization measurements. At lower energy, extra peaks are observed; they can be assigned to the biexciton and charged excitons.

To analyze the low energy peaks, a study of the  $\mu$ -PL spectrum, versus the excitation intensity, has been performed on a QD with a 1 nm nominal thickness. Figure 2(d) shows the excitation power dependence of the QD emission intensity for the peaks at 1643.5 and 1647.7 meV. When  $P_{exc}$  is large, both emission intensities saturate, as expected. Below saturation, from a power law fit ( $I \propto P_{exc}^\alpha$ ), it can be seen that the neutral exciton emission has a linear dependence on the excitation power whereas the line at 1643.5 meV has a quadratic dependence which is the signature of the biexciton ( $XX$ ) complex. The inter-

mediate emission, between  $X$  and  $XX$ , can be attributed to charged excitons (as we will discuss below).

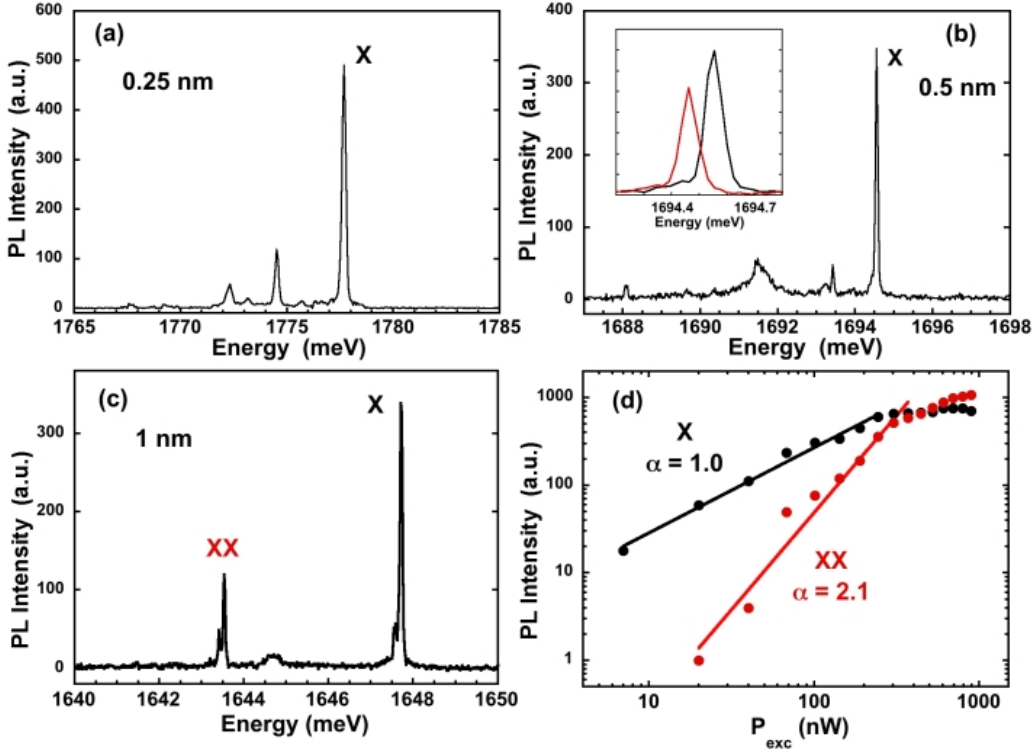


FIG. 2: (a)-(c)  $\mu$ -PL spectra of single QDs with different sizes. The nominal thickness is given for each QD. The highest energy line for each dot is the neutral exciton emission, characterized by polarisation measurements not shown here; inset (b) shows orthogonally polarised exciton emission. (d) Intensity of the exciton (black dot) and biexciton (red dot) emission lines, respectively at 1647.7 and 1643.5 meV ; a power law fit, below saturation, leads to the exponents  $\alpha = 1.0$  and 2.1, respectively.

## 2.2. Theoretical model

We first model the QD shape and then calculate the single particle energy levels, the single particle wave functions (WFs) and the final alignment of the excitonic states by combining a good description of the QD shape and the BenDaniel-Duke Hamiltonian [19]. Since a shape anisotropy induces a splitting of  $p$ -like states, we also calculate the  $s$ - $p_x$  ( $\Delta_{s-p_x}$ ) and  $s$ - $p_y$  ( $\Delta_{s-p_y}$ ) energy level spacings.

### 2.2.1. Shape modelling

The QDs studied here differ from the symmetric GaAs/AlGaAs QDs that we have previously modelled [15] in that the dots here are elongated along the  $(Ox)$  ( $[110]$ ) direction (see Fig. 1 Ref. [7]). It is however possible to adapt the QD shape modelling approach used in Ref. [15] to take into account the QD shape anisotropy as described in Fig. 3. The QDs are modelled by the overlaying of two ellipsoids  $E_1$  and  $E_2$  revolving around the  $z$  axis (the growth direction) with different centers and eccentricities.  $E_1$  ( $E_2$ ) describes the shape of NH before (after) GaAs filling. These ellipsoids satisfy the following equations:

$$\frac{r_{ix}^2}{a_{0i}^2} + \frac{r_{iy}^2}{b_{0i}^2} + \frac{(z + d_i)^2}{c_{0i}^2} = 1 \quad (1)$$

the indices  $i = 1$  and  $i = 2$  are reserved for NH before and after filling, respectively.

Note that in the symmetric QD case, the cross-section of the two ellipsoids and  $(xOy)$  planes are circles, while they are ellipses of radii  $R_b(\theta, z)$  for the asymmetric QD case :

$$R_b(\theta, z) = \frac{1}{\sqrt{\frac{\cos^2 \theta}{r_{ix}^2} + \frac{\sin^2 \theta}{r_{iy}^2}}} \quad (2)$$

where  $r_{ix}$  and  $r_{iy}$  are the major and minor ellipse axes, respectively. They are defined as follows:

$$\begin{aligned} r_{ix}^2(z) &= a_{0i}^2 \left( 1 - \frac{(z + d_i)^2}{c_{0i}^2} \right) \\ r_{iy}^2(z) &= b_{0i}^2 \left( 1 - \frac{(z + d_i)^2}{c_{0i}^2} \right) \end{aligned} \quad (3)$$

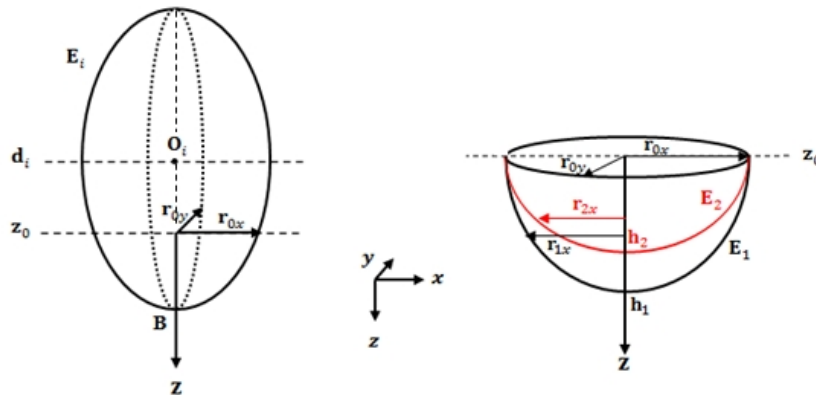


FIG. 3: Schematic view of the QD shape modeling.

In order to determine the other parameters, namely  $a_{0_i}$ ,  $b_{0_i}$ ,  $c_{0_i}$  and  $d_i$ , the same approach as in Ref. [15] is followed. We note that the QD dimensions were based on the AFM data of the AlGaAs NH before and after GaAs filling [7]. These AFM measurements establish that the hole opening is anisotropic and the profiles allow us to define an aspect ratio  $\beta = \frac{r_{0x}}{r_{0y}} \approx 2.5$ , where  $r_{0x}$  and  $r_{0y}$  are the radii of the hole opening along the major axis ( $x = [110]$ ) and the minor axis ( $y = [\bar{1}10]$ ) for the elongated structure, respectively. The NH depth before GaAs filling is  $h_1 \approx 8$  nm and we denote by  $h_2$  the NH depth after filling. Thus, the QD height is defined as  $h_{QD} = (h_1 - h_2)$ .  $h_2$  is considered as an adjustable parameter in our calculations.

### 2.2.2. Confined states : outline of the calculation method

To calculate the charge carrier states within the effective-mass theory, we consider the single carrier (electron (e) or hole (h)) Hamiltonian which is written as follows:

$$\mathcal{H}_{e(h)} = \mathcal{T}_{e(h)}(\mathbf{r}_{e(h)}) + \mathcal{V}_{e(h)}^{conf}(\mathbf{r}_{e(h)}) \quad (4)$$

where  $\mathcal{V}_{e(h)}^{conf}(\mathbf{r}_{e(h)})$  is the carrier confinement potential and  $\mathcal{T}(\mathbf{r}_{e(h)})$  denotes the carrier kinetic operator. Taking into account the QD shape anisotropy, the cylindrical symmetry is somewhat broken and, in this case, the kinetic energy operator will be decomposed into three components as follows:

$$\mathcal{T}_{e(h)} = \mathcal{T}_{e(h)}^z + \mathcal{T}_{e(h)}^\rho + \mathcal{T}_{e(h)}^\theta \quad (5)$$

with

$$\begin{cases} \mathcal{T}_{e(h)}^z = -\frac{\hbar^2}{2} \left[ \frac{\partial}{\partial z} \frac{1}{m_{e(h)}^z} \frac{\partial}{\partial z} \right] \\ \mathcal{T}_{e(h)}^\rho = -\frac{\hbar^2}{2} \left[ \frac{1}{\rho} \frac{\partial}{\partial \rho} \frac{\rho}{m_{e(h)}^\rho} \frac{\partial}{\partial \rho} \right] \\ \mathcal{T}_{e(h)}^\theta = -\frac{\hbar^2}{2} \left[ \frac{1}{\rho^2} \frac{\partial}{\partial \theta} \frac{1}{m_{e(h)}^\rho} \frac{\partial}{\partial \theta} \right] \end{cases} \quad (6)$$

where  $(\rho, \theta, z)$  denotes cylindrical coordinates.  $m_{e(h)}^z$  and  $m_{e(h)}^\rho$  are the carriers effective masses along  $z$ - and  $\rho$ - directions, respectively. The Luttinger parameters,  $\gamma_j$  ( $j = 1, 2$ ) are calculated via the 40-band  $\mathbf{k}\cdot\mathbf{p}$  theoretical model [20]. The numerical parameters used in our calculations are compiled in Table 1.



GaAs					GaAs/Al <sub>0.45</sub> Ga <sub>0.55</sub> As		
$\gamma_1$	$\gamma_2$	$m_e(m_0)$	$m_h^z(m_0)$	$m_h^p(m_0)$	$\varepsilon$	$V_e(\text{eV})$	$V_h(\text{eV})$
7.03	2.33	0.067	0.422	0.107	12.47	0.390	0.206

TABLE I: Numerical values of the input parameters used in this work. Masses are given in free electron mass unit

The carriers energy levels are calculated by diagonalizing the Hamiltonian  $\mathcal{H}_{e(h)}$  using the matrix method over a known and finite eigenstate basis. The eigenfunctions of the Hamiltonian are expanded in a Fourier-Bessel finite series as  $\Psi_n(\mathbf{r}_{e(h)}) = \sum_{\ell>0, m>0}^{\ell_{\max}, m_{\max}} C_{\ell m}^n \phi_{\ell m}^n(\rho_{e(h)}, \theta_{e(h)}, z_{e(h)})$ , with  $C_{\ell m}^n$  are the basis coefficients. The  $\phi_{\ell m}^n(\rho_{e(h)}, \theta_{e(h)}, z_{e(h)})$  functions correspond to the eigenbasis of a large cylinder of height  $Z_C$  and elliptical base of radius  $\mathcal{R}_C(\theta)$  which is given by :  $\mathcal{R}_C(\theta) = 1/(\sqrt{\frac{\cos^2\theta}{A^2} + \frac{\sin^2\theta}{B^2}})$ . A and B denote the dimensions along x- and y- directions of the elongated cylinder, respectively. The normalization condition of the carriers WFs imposes the condition  $(A/B) = \beta = 2.5$ . The origin of the z-axis is taken at the midpoint of the cylinder.  $\phi_{\ell m}^n$  are given by:

$$\left\{ \begin{array}{l} \phi_{\ell m}^0(\rho_{e(h)}, \theta_{e(h)}, z_{e(h)}) = \alpha_\ell^0 J_0\left(\frac{\lambda_\ell^0}{\mathcal{R}_C(\theta)}\rho_{e(h)}\right) \sin\left(\frac{\pi m}{Z_C}z_{e(h)}\right), \text{ for } s\text{-state} \\ \phi_{\ell m}^1(\rho_{e(h)}, \theta_{e(h)}, z_{e(h)}) = \alpha_\ell^1 \left(\frac{A+B}{A}\right)^{1/2} \cos(\theta_{e(h)}) J_1\left(\frac{\lambda_\ell^1}{\mathcal{R}_C(\theta)}\rho_{e(h)}\right) \sin\left(\frac{\pi m}{Z_C}z_{e(h)}\right), \text{ for } p_x\text{-state} \\ \phi_{\ell m}^{-1}(\rho_{e(h)}, \theta_{e(h)}, z_{e(h)}) = \alpha_\ell^{-1} \left(\frac{A+B}{B}\right)^{1/2} \sin(\theta_{e(h)}) J_{-1}\left(\frac{\lambda_\ell^{-1}}{\mathcal{R}_C(\theta)}\rho_{e(h)}\right) \sin\left(\frac{\pi m}{Z_C}z_{e(h)}\right), \text{ for } p_y\text{-state} \end{array} \right. \quad (7)$$

$\lambda_\ell^n$  is the  $\ell^{\text{th}}$  root of the n-order Bessel functions  $J_n$ , and  $\alpha_\ell^n$  are the normalization constants.

We should point out that only the matrix elements of the kinetic term  $\mathcal{T}_{e(h)}^\theta$  are affected by the QD shape anisotropy, and these are calculated using Eq. (6) and (7). Calculations show that these elements differ from one state to another. The other contributions of the kinetic matrix elements,  $\mathcal{T}_{e(h)}^z$  and  $\mathcal{T}_{e(h)}^p$  are given in Ref. [21].

Thus, finding the exact energy eigenvalues of the stationary Schrödinger equation is reduced to the numerical diagonalization of the Hamiltonian matrix. Such a technique has proved itself to be a workable and reliable approach [22, 23].

### 3. Results

In this section, we check the accuracy of our numerical approach by comparing the theoretical results with experimental data. Firstly, we begin by calculating the carriers confinement energies as well as the  $s - p_{x(y)}$  and  $p_x - p_y$  spacing energies, supported by a study of the carriers WFs distribution and localization inside the QD. We then calculate the binding energies of the excitonic complexes present in the dot, such as the neutral excitons, charged excitons ( $X^+$  and  $X^-$ ) and the biexcitons. This is then compared with  $\mu$ -PL data on single dots with different heights. A study of the anisotropic FSS of the ground state (s-s) exciton concludes the section.

#### 3.1. Single-particle energy levels

As described previously, the electron and hole energy levels are numerically calculated by diagonalizing  $\mathcal{H}_{e(h)}$  over the eigenstates basis of a large cylinder. Note that, due to symmetry conditions, the cylinder is laterally elongated with an anisotropy factor equal to that of the QD:  $\beta = \frac{A}{B} = \frac{r_{0x}}{r_{0y}} = 2.5$ . Figure 4(a) shows the electron and hole confinement energies of the  $s$ -shell ( $E_s^{e(h)}$ ),  $p_x$ -shell ( $E_{p_x}^{e(h)}$ ) and  $p_y$ -shell ( $E_{p_y}^{e(h)}$ ) states as a function of  $h_{QD}$ . As for conventional QDs, the carriers confinement energies of the studied QDs decrease gradually when increasing the QD size. In contrast to the case of symmetric QDs [15] and as expected a degeneracy lifting of the p-shell states is observed for asymmetric QDs. In Fig. 4(b), we highlight the size effect on the  $s-p_x$  and  $s-p_y$  level spacing energies  $\Delta E_{s-p_x}^{e,h}$  and  $\Delta E_{s-p_y}^{e,h}$ , respectively. It is known that the energy spacing mainly depends on the lateral size. For the studied QDs, the increase of the QD height leads to an expansion of the QD lateral size due to the shape of the NH and an increase of the WF extensions (see Fig. 6). This explains the decrease of  $\Delta E_{s-p_x}^{e,h}$  and  $\Delta E_{s-p_y}^{e,h}$  as  $h_{QD}$  increases, as well as the  $p_x-p_y$  spacing energy becoming equal to a few meV.

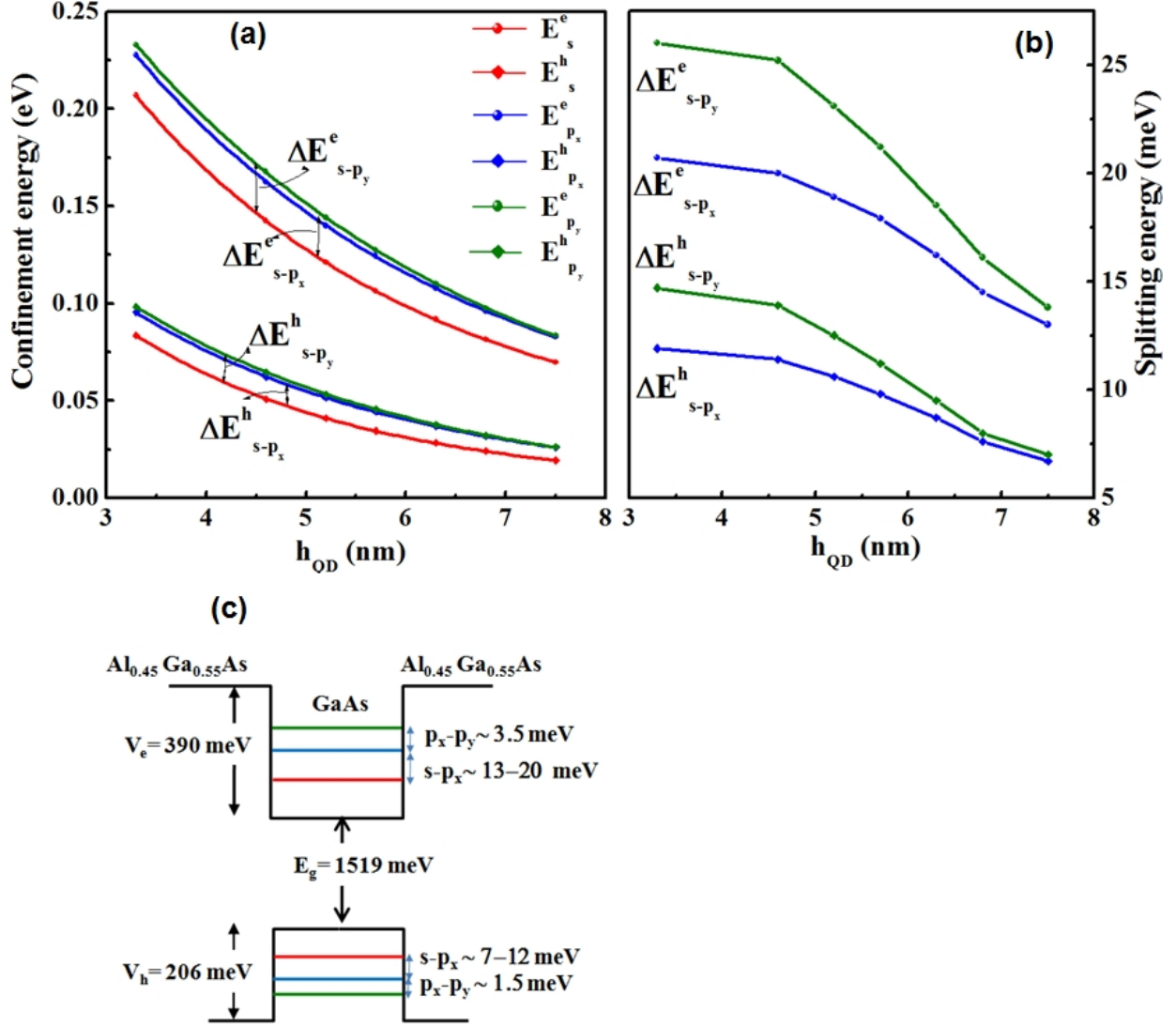


FIG. 4: (a) Calculated single particle, electron and hole, confinement energies of the  $s$ ,  $p_x$  and  $p_y$  states with respect to  $h_{QD}$ . (b) Calculated  $s$ - $p_x$  and  $s$ - $p_y$  splitting energies of electrons and holes as a function of  $h_{QD}$ . (c) Band alignment of the GaAs/Al<sub>0.45</sub>Ga<sub>0.55</sub>As QD. The  $s$ - $p_x$  and  $p_x$ - $p_y$  splitting energies are shown for both electron and hole

This is summarized in Fig. 4(c) which shows a schematic illustration of single-particle electron and hole energy levels for the GaAs/AlGaAs QDs studied here. We have neglected here the fact that the as-grown QDs had a lower Al<sub>0.45</sub>Ga<sub>0.55</sub>As barrier and an upper Al<sub>0.33</sub>Ga<sub>0.67</sub>As barrier, treating both barriers as Al<sub>0.45</sub>Ga<sub>0.55</sub>As. The  $s - p_x$  energy spacing ranges between 6.7 meV and 11.7 meV for holes, while for electrons it is almost double. The

$p_x - p_y$  spacing energy is much lower than  $s - p_x$  one.

### 3.2. Electron and hole wave functions distribution

WFs of single charge carriers are calculated by solving the Schrödinger equation. We denote by  $|\Psi_n^{e(h)}(x)|^2$ ,  $|\Psi_n^{e(h)}(y)|^2$  and  $|\Psi_n^{e(h)}(z)|^2$  the electron or hole densities along ( $x = [110]$ ), ( $y = [\bar{1}10]$ ) and ( $z = [001]$ )-axes, respectively.  $n = 0, 1$  and  $-1$  indicate  $s$ ,  $p_x$  and  $p_y$ -states, respectively. Our numerical results for a given QD ( $r_{0x}=75$  nm,  $r_{0y}=30$  nm) are shown in Fig. 5.

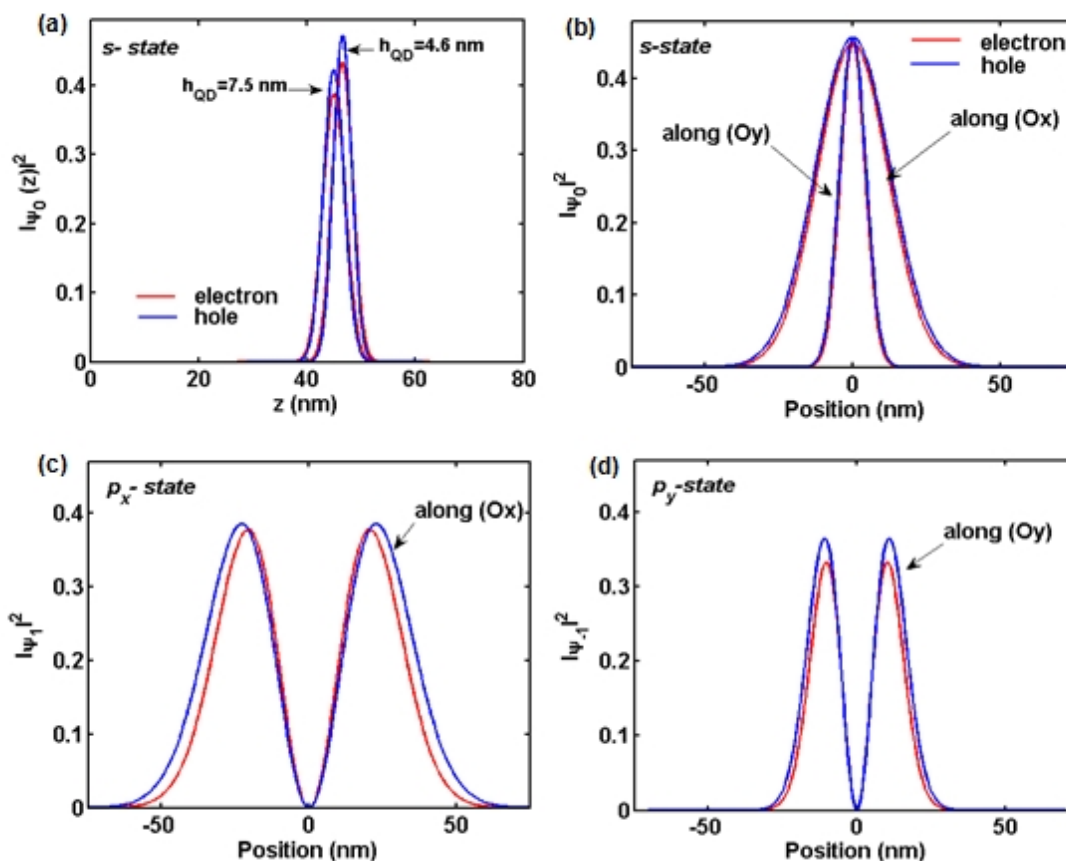


FIG. 5 : Electron and hole WFs of GaAs/Al<sub>0.45</sub>Ga<sub>0.55</sub>As QDs with  $r_{0x}=75$  nm and  $r_{0y}=30$  nm. (a) Evolution of  $|\Psi_0^{e(h)}(z)|^2$  with respect to  $h_{\text{QD}}$ . (b)-(d) The distribution of  $s$ ,  $p_x$  and  $p_y$  carriers WFs in the in-plane directions.

These plots show that: (i) the electron and hole WFs are highly localized inside the GaAs QD, and (ii) the distribution of the carriers WFs, for a given state, reflects the anisotropy

and the size of the QD. Plots of the  $s$ ,  $p_x$  and  $p_y$  WFs along  $(Ox)$  and  $(Oy)$  directions are presented in Figs. 5(b), (c) and (d), respectively.

In order to show more clearly the evolution of the WFs extension with the QD height, we have reproduced the carriers' WFs by Gaussian fits using the following expressions [24]:

$$\left\{ \begin{array}{l} \left| \Psi_0^{e(h)} \right|^2 = A_{e(h)}^0 e^{-\frac{x_e^2(h)}{\ell_{x_e(h)}^2}} e^{-\frac{y_e^2(h)}{\ell_{y_e(h)}^2}} e^{-\frac{(z_{e(h)}-z_{m_{e(h)}})^2}{\ell_{z_{e(h)}^2}}}, \text{ for } s\text{-state} \\ \left| \Psi_1^{e(h)} \right|^2 = A_{e(h)}^1 x_e^2(h) e^{-\frac{x_e^2(h)}{\ell_{x_e(h)}^2}} e^{-\frac{y_e^2(h)}{\ell_{y_e(h)}^2}} e^{-\frac{(z_{e(h)}-z_{m_{e(h)}})^2}{\ell_{z_{e(h)}^2}}}, \text{ for } p_x\text{-state} \\ \left| \Psi_{-1}^{e(h)} \right|^2 = A_{e(h)}^{-1} y_e^2(h) e^{-\frac{x_e^2(h)}{\ell_{x_e(h)}^2}} e^{-\frac{y_e^2(h)}{\ell_{y_e(h)}^2}} e^{-\frac{(z_{e(h)}-z_{m_{e(h)}})^2}{\ell_{z_{e(h)}^2}}}, \text{ for } p_y\text{-state} \end{array} \right. \quad (8)$$

where  $A_{e(h)}^n$  ( $n = 0, \pm 1$ ) are the normalization constants.  $\ell_{x_{e(h)}}$ ,  $\ell_{y_{e(h)}}$  and  $\ell_{z_{e(h)}}$  are the fit parameters which determine the  $e(h)$ - WFs extension in the three directions  $x$ ,  $y$  and  $z$ .

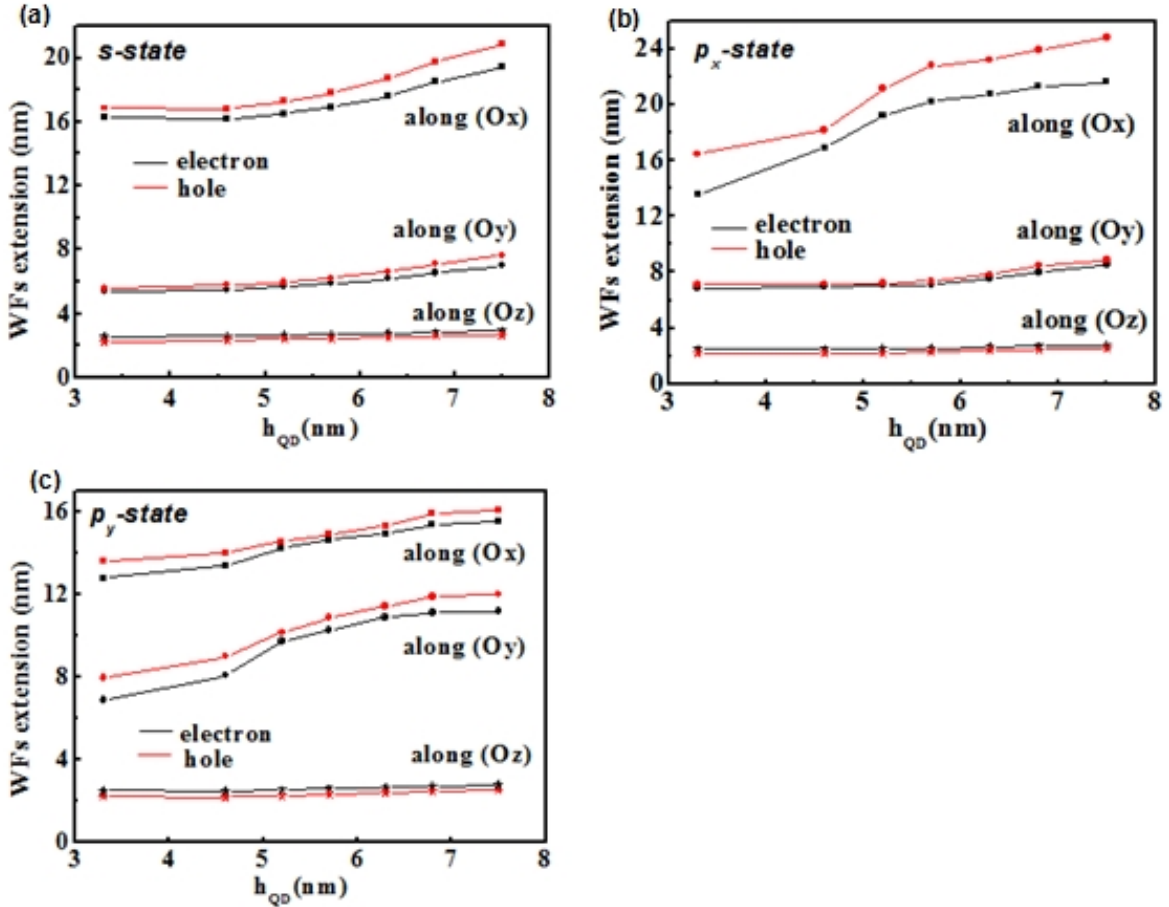


FIG. 6: (a)-(c) The evolution of the  $s$ ,  $p_x$  and  $p_y$  carriers WFs extension with respect to  $h_{QD}$ .

It can be seen from Fig. 6(a)-(c) that the WF extension always decreases as the QD size decreases. The WF extension along ( $Oz$ ) is similar for all the states, due to the fact that the main confinement is along the ( $Oz$ ) direction. In the  $xOy$  plane, the WF is always elongated along ( $Ox$ ) reflecting the dot asymmetry; however the increase in WF extension with dot height is more rapid along the ( $Ox$ ) direction than the ( $Oy$ ) direction for the  $p_x$ -state so that the  $p_x$  state become more anisotropic, and more rapid along the ( $Oy$ ) direction compared to the ( $Ox$ ) direction for the  $p_y$ -state such that the  $p_y$  state becomes more isotropic.

### 3.3. Exciton transition energy: comparison with experiment

In this section, we compare the ground state transition energy,  $E_0(X)$  experimentally observed, with our numerical results. The exciton energy can be calculated as follows:

$$E_0(X) = E_g + E_0^e + E_0^h - |V_{eh}^0| \quad (9)$$

where  $E_g$  is the GaAs QD band gap energy. The electron and hole confinement energies,  $E_0^e$  and  $E_0^h$ , are defined relative to the bottom of the confinement potential.  $V_{eh}^0$  is the electron-hole Coulomb energy treated in the perturbative approach and it is given by [25]:

$$V_{eh}^0 = -\frac{e^2}{4\pi\epsilon_0\epsilon} \iint \frac{|\Psi_0^e(\vec{r}_e)|^2 |\Psi_0^h(\vec{r}_h)|^2}{|\vec{r}_e - \vec{r}_h|} d^3\vec{r}_e d^3\vec{r}_h \quad (10)$$

where  $\epsilon$  is the average dielectric constant of GaAs [26].

In Fig. 7(a), we show the dependence of the QD emission energy as a function of the dot height  $h_{QD}$  ( $h_{QD} = (8 \text{ nm} - h_2)$ , where 8 nm is the average NH depth, and  $h_2$  is an input to the calculation). The calculated QD emission energy can then be compared to the measured ensemble QD emission energy for a given nominal thickness, which allows the QD height for a given nominal thickness to be estimated. This is shown in Fig. 7(b), where the experimental data points of ensemble emission *vs.* nominal GaAs thickness is shown, together with the estimated QD height *vs.* nominal thickness taken from the calculated emission energies. It can be seen that the QD height is much greater than the nominal thickness due to the fact that there is net migration towards the bottom of the nanohole.

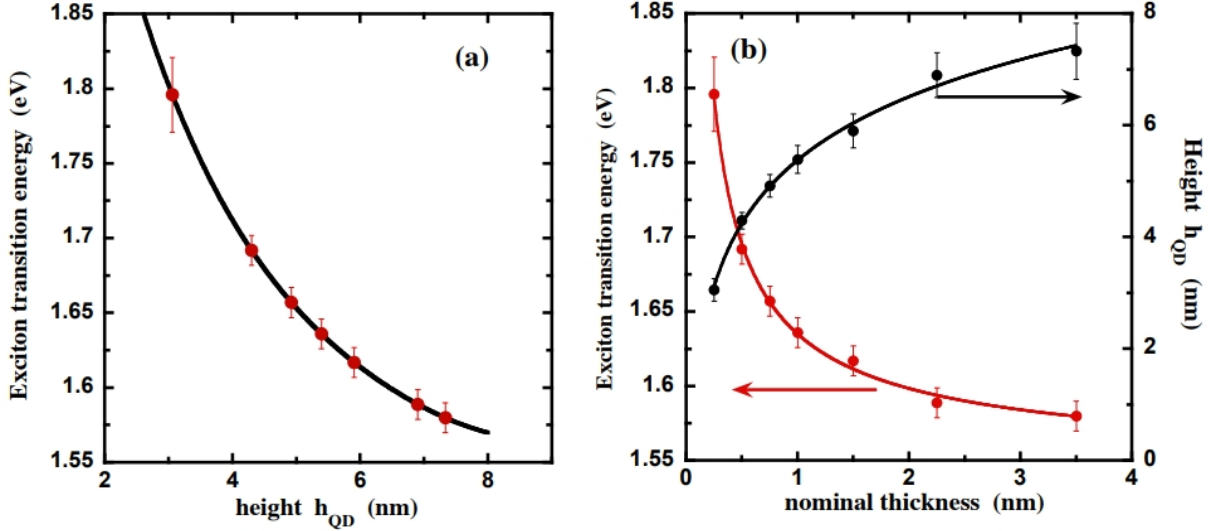


FIG. 7: (a) Calculated (black curve) and measured (red points) excitonic transition energy of the ground state. (b) Measured excitonic transition energy as a function of the nominal GaAs thickness deposited (red points), and corresponding calculated QD height ( $h_{QD}$ ) (black points). The curves are guides to eye.

### 3.4. Excitonic complexes binding energies

We present a systematic calculation of the few-particle binding energies in order to assign excitonic complexes to the peaks observed in single QD  $\mu$ -PL spectra. We first calculate the excitonic complexes binding energies in terms of direct Coulomb interactions and then the effect of correlation energies will be included. The electron-hole exchange interaction effects on the excitonic binding energy will be discussed thereafter.

The s-shell direct Coulomb interactions between an electron and a hole ( $V_{eh}^0$ ), and between two electrons ( $V_{ee}^0$ ) and two holes ( $V_{hh}^0$ ) are calculated using Eq. (10), and plotted as a function of  $h_{QD}$  in Fig. 8(a).

All these quantities decrease when  $h_{QD}$  increases which is attributed to the reduced overlap of the carriers WFs and the increase of the WFs extension already noted in Fig. 6. It can also be seen that the hole-hole Coulomb interaction is always smaller than the electron-electron interaction. This can be explained by the larger extension of the hole WF in the ( $Ox$ ) and ( $Oy$ ) directions compared to that of the electron (see Fig. 6(a)). Our results satisfy the following relationship [27]:  $V_{ee}^0 > |V_{eh}^0| > V_{hh}^0$  over the entire dot height range studied here. This finding is in contrast to the symmetric QDs case where a change

in order of the Coulomb contributions was observed [15]. The absence of such a reversal in the asymmetric QDs studied here is mainly due to the larger lateral dimensions of the dot. Both electron and hole carriers are confined within even the thinnest QDs, and their WFs evolve in a monotonic way which explains the monotonic behavior of  $V_{ee}^0$ ,  $|V_{eh}^0|$  and  $V_{hh}^0$  with respect to  $h_{QD}$ .

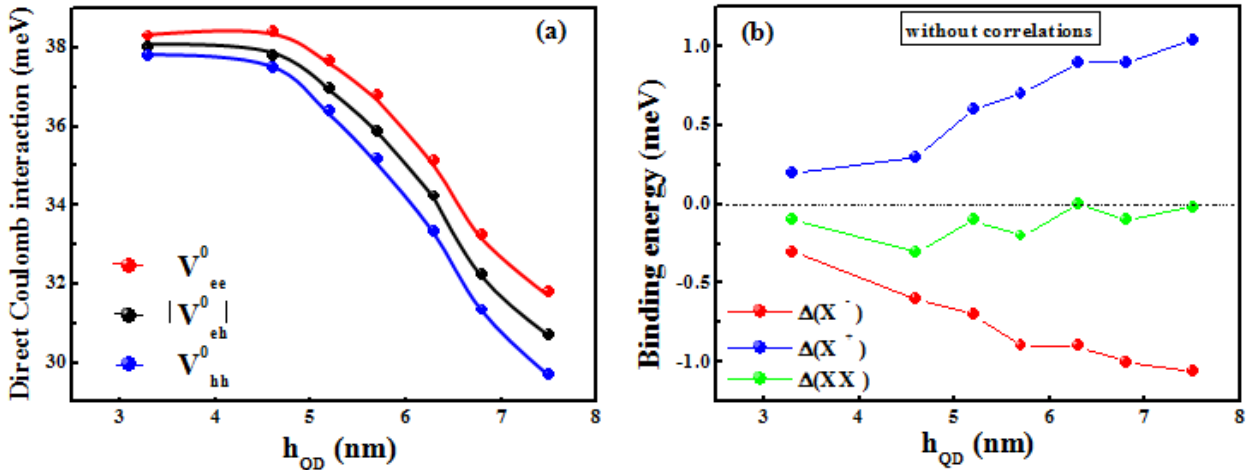


FIG. 8: (a) Direct Coulomb interactions versus  $h_{QD}$ . (b) Calculated binding energies of exciton complexes as a function of  $h_{QD}$  without including correlation effects.

We denote by  $\Delta(X^\ell)$  ( $\ell = \pm$ ) the binding energy of trions and by  $\Delta(XX)$  that of biexcitons. These quantities have been estimated using the Hartree-Fock approximation in terms of direct Coulomb energies (see Eq. (6) of Ref. [15]). Figure 8(b) shows the evolution of  $\Delta(X^\ell)$  and  $\Delta(XX)$  as a function of  $h_{QD}$ . The important points in this figure are summarized as follows: (i)  $\Delta(X^-)$  is always negative, thus  $X^-$  forms an unbound state.  $\Delta(X^-)$  becomes more negative as  $h_{QD}$  increases. (ii)  $X^+$  shows a trend opposite to  $X^-$ . Its binding energy increases with QD height and it is positive, meaning that  $X^+$  forms a bound state. (iii)  $XX$  shows a binding energy close to zero, regardless of  $h_{QD}$ . Since the binding energy of a few-particle state is approximated by the sum of attractive and repulsive interactions between all pairs of particles, the same magnitude of the  $\Delta(X^-)$  and  $\Delta(X^+)$  but with opposite trends is expected. This result agrees well with the  $V_{ee}^0$ ,  $|V_{eh}^0|$  and  $V_{hh}^0$  ordering seen in Fig. 8(a). It is important to note however that the few-particle binding energies cannot be fully evaluated using only the direct Coulomb interaction. Consideration of the correlation effects is paramount to provide a good estimation of the excitonic complexes



binding energies. This has been demonstrated in several previous works either in strained QDs [28] or unstrained ones [6, 15].

In the following, we calculate the few-particle binding energies by evaluating the Coulombic interaction expressions to the second order of the perturbation theory. The procedure is detailed in Ref. [15] (Eqs (7)-(9)). We have summarized our theoretical results of the correlation energies ( $\delta_c(X)$ ,  $\delta_c(X^\ell)$  ( $\ell = \pm$ ), and  $\delta_c(XX)$ ) as well as the binding energies ( $\Delta_c(X^\ell)$  ( $\ell = \pm$ ),  $\Delta_c(XX)$ ) of the excitonic complexes in Figs. 9(a) and 9(b), respectively.

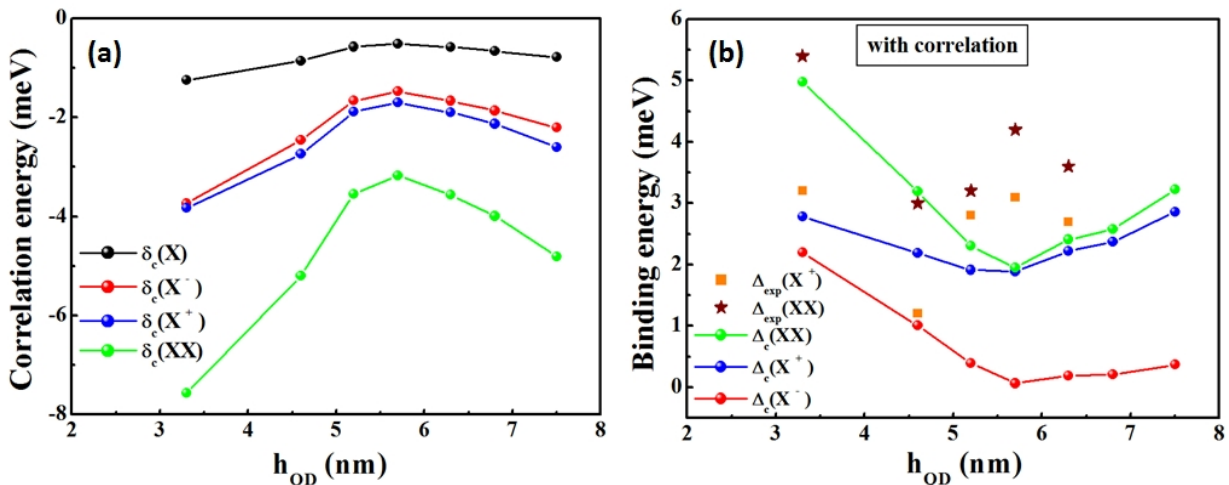


Fig. 9: (a) The variation of the correlation energies of the exciton complexes as well as the neutral exciton,  $\delta_c$ , with respect to  $h_{QD}$ . (b) Calculated binding energies of exciton complexes as a function of  $h_{QD}$  while including correlation effects. The wine-coloured stars indicate the  $\mu$ -PL experimental data.

It can be seen that the few-particle correlation energies and binding energies are mutually correlated. A sensitive dependence of the correlation energies on the  $h_{QD}$  is plainly shown in Fig. 9(a). Compared to the symmetric QDs case where the set of the correlation energies ( $\delta_c$ ) vary monotonically with the QD height, in asymmetric QDs the correlation energies first increase and then subsequently decrease with increasing height because  $\delta_c$  depends both on the  $s - p$  splitting energies and the Coulomb interaction energies  $V_{ij}^{n_i m_j 00}$ , (see Eq. (7) of Ref. [15]). The Coulomb coupling  $V_{ij}^{n_i m_j 00}$  depends strongly on the WF overlap and extension. From our study (see Fig. 6), the WF extensions are continuously increasing and so  $|V_{ij}^{n_i m_j 00}|$  is continuously decreasing, with increasing  $h_{QD}$ . For the  $s-p$  splittings,  $\Delta E_{s-p_x(y)}$ , we observe two regimes (see Fig. 4(b)): below 5 nm, the splitting is almost constant,

while at higher QD thickness, this splitting decreases rapidly. The correlation term being proportional to  $\left|V_{ij}^{n_i m_j 00}\right|^2$  and inversely proportional to  $\Delta E_{s-p_x(y)}$ , one can conclude that at low thickness ( $\Delta E_{s-p_x(y)}$  almost constant), the correlation term decreases following the Coulomb contribution, while at high thickness, the rapid decrease of  $\Delta E_{s-p_x(y)}$  leads to an increase of  $|\delta_c|$ .

We present in Fig. 9(b) the calculated binding energies when including correlation effects. It is clear that all the calculated few-particles binding energies are now positive, consistent with experimental observations. The addition of the correlation effects leads to a change from unbound to bound for  $X^-$  and  $XX$  states as was previously shown for symmetric GaAs QDs [15]. The sequence of excitonic peaks, arranged in order of increasing emission energy is  $XX$ ,  $X^+$ ,  $X^-$ ,  $X$  and is similar to that obtained for bow-tie shaped GaAs QDs, where the  $X^+$  was also found to have a binding energy of around 3 meV [17]. In contrast,  $X^+$  is typically unbound in strained InAs QDs [27]. This difference can be related to the larger lateral size of the GaAs QDs, which increases the contribution of the correlation effect on the exciton binding energy resulting in a bound positive trion for these dots [15, 31].

$\mu$ -PL measurements of QDs show a strong emission associated with the neutral exciton and two weaker lines at lower energy (see Fig. 2). The main emission line is attributed to the exciton  $X$ . The lowest energy line is attributed to the biexciton  $XX$ , since its emission intensity shows a quadratic dependence on the excitation power. This observation is in agreement with our calculations, which predicts that  $XX$  has the highest binding energy. The theoretical binding energies, for all the excitonic complexes are plotted on Fig. 9(b) together with the experimental values for  $XX$ . Our calculations reproduce quite well the  $XX$  binding energy which is in the 3 – 5 meV range. While a good agreement is obtained for low QD thickness, a discrepancy is observed at high QD thickness ( $h_{QD} > 5.5$  nm). This deviation is related to the smaller  $s$  and  $p$ -states splitting when  $h_{QD}$  increases and the fact that the contribution of the  $d$ -states has not been included in these calculations. Finally, for the intermediate emission line, the binding energy varies from 1.3 to 3.2 meV, with a mean value equal to 2.6 meV. This allows this emission line to be assigned to the positively charged exciton  $X^+$ , according to our calculation.

### 3.5. Exchange interaction effects: fine structure splitting

Here, we study the role of the e-h exchange interaction taking into account the shape anisotropy, on the excitonic properties. In particular, we investigate the contribution of the long-range exchange interaction which can be separated into two different terms acting on bright exciton states: (i) a diagonal term ( $\varepsilon_d^{exch}$ ) which induces an additional energy correction, the same for both bright excitons; (ii) the off-diagonal term ( $\varepsilon_{od}^{exch}$ ) which splits the bright excitons and will give the exciton fine-structure splitting:  $FSS = 2 |\varepsilon_{od}^{exch}|$ .  $\varepsilon_d^{exch}$  and  $\varepsilon_{od}^{exch}$  are given by

$$\varepsilon_d^{exch} = \frac{\hbar^2}{4m_0} \frac{E_P}{E_g^2} \int dq (q_x^2 + q_y^2) V_q \left| \int d^3\mathbf{r} \psi_{n_e}^*(\mathbf{r}) \psi_{n_h}(\mathbf{r}) e^{i\mathbf{q}\cdot\mathbf{r}} \right|^2 \quad (11)$$

$$\varepsilon_{od}^{exch} = \frac{\hbar^2}{4m_0} \frac{E_P}{E_g^2} \int dq (q_x + iq_y)^2 V_q \left| \int d^3\mathbf{r} \psi_{n_e}^*(\mathbf{r}) \psi_{n_h}(\mathbf{r}) e^{i\mathbf{q}\cdot\mathbf{r}} \right|^2 \quad (12)$$

where  $E_P = 23.81$  eV [20] is the related energy to the Kane matrix element  $P = \frac{\hbar}{m_0} \langle S | p_x | iX \rangle = \frac{\hbar}{m_0} \langle S | p_y | iY \rangle = \frac{\hbar}{m_0} \langle S | p_z | iZ \rangle$ .  $V_q = -\frac{1}{(2\pi)^3} \frac{e^2}{\varepsilon_0 \varepsilon_r q^2}$  is the Fourier transform of the Coulomb potential. We then evaluate numerically,  $\varepsilon_d^{exch}$  and  $\varepsilon_{od}^{exch}$  by using the Gaussian functions. It should be noted that previous studies on III-V QDs have shown that both the short range exchange interaction and the contribution of the valence band mixing to the long range exchange interaction have only a very weak effect on the magnitude of the bright exciton splitting, and so these effects have not been included here [30].

Our calculations show that the correction to the exciton binding energy due to e-h exchange interaction,  $|\varepsilon_d^{exch}|$ , ranges between 14  $\mu\text{eV}$  and 30  $\mu\text{eV}$  (inset of Fig. 10). The magnitude of this term is quite negligible, in comparison with the other contributions (direct Coulomb interaction and correlation energy) and consequently, it does not impact on the excitonic binding energy. We show in Fig. 10 calculated and measured FSS values as a function of the  $X$  emission energy. The FSS has been measured on 5 QD families, with emission energy ranging from 1.58 to 1.72 eV. The FSS varies from 17 to 155  $\mu\text{eV}$ . In contrast, GaAs/AlGaAs QDs grown in quasi-symmetric LDE nanoholes [10] showed a FSS varying from 4 to 12  $\mu\text{eV}$ , for the same exciton energy range. For the same QD size, one then observes a FSS one order of magnitude larger, signature of the asymmetric nanohole shape. Our calculations predict a FSS increase from 16 to 36  $\mu\text{eV}$  for the same energy range, which qualitatively agrees with the experimentally increase of the FSS observed here,

and on other quasi-isotropic [10] or anisotropic [31] GaAs/AlGaAs QDs. A quantitative agreement is missing for the thinnest QDs. For small nominal thicknesses, the QD shape will strongly depend on the NH bottom, whose symmetry is probably reduced under the effect of inhomogeneous etching at the start of the droplet etching process. Moreover, as shown on AFM images (Fig. 1), the profile along  $(Oy)$  is not symmetric meaning that the  $xOz$  plane is no more a mirror plane: the  $C_{2v}$  symmetry, assumed in our model, is broken to a  $C_s$  symmetry. This extra anisotropy may favor an increase of the FSS in small QDs, needing more complex calculations.

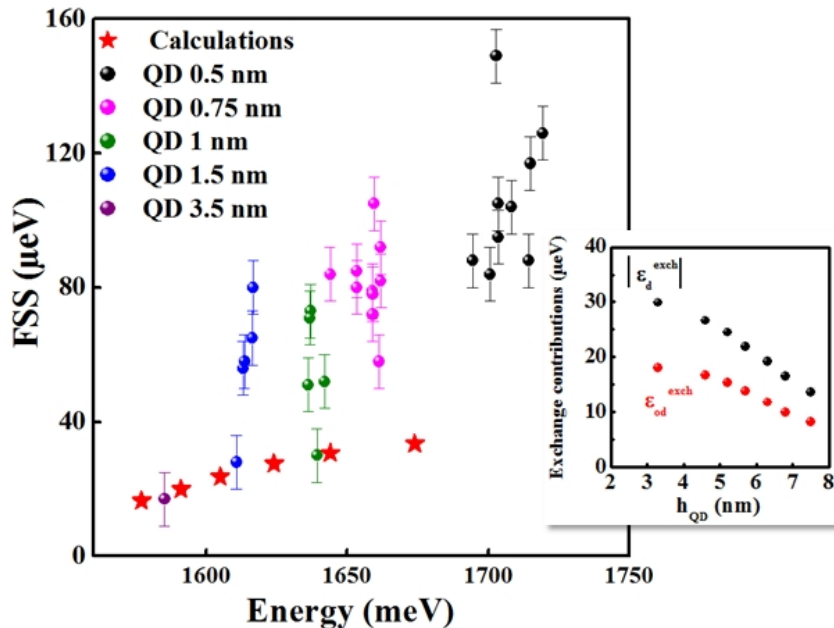


Fig. 10: Calculated (stars) and measured (circles) values of the FSS as a function of the  $X$  emission energy for different QDs. The inset shows the calculated values of the diagonal ( $|\epsilon_d^{exch}|$ ) and off-diagonal ( $\epsilon_{od}^{exch}$ ) terms of the long-range exchange interaction as a function of  $h_{QD}$ .

#### 4. Conclusions

We present here an experimental and theoretical study of the electronic states of asymmetric strain-free GaAs/AlGaAs QDs grown by the local droplet etching and infilling method. Both the lateral and vertical size of these QDs can be adjusted by the thickness of the filling layer. AFM data allowed us to give a realistic description of the anisotropic QD shape. Using the effective mass approximation and the BenDaniel-Duke Hamiltonian, we have pro-

vided a detailed calculation of the charge carriers energy levels which includes new terms, compared to the symmetric case, arising from the shape anisotropy. The calculated exciton transition energies correspond to realistic dot heights in the nanoholes, demonstrating the suitability of our theoretical approach. For a series of QD height ranging between  $3.3 \text{ nm} < h_{QD} < 7.5 \text{ nm}$ , the emission energy of the QD  $s$ -state decreases from  $1.77 \text{ eV}$  to  $1.57 \text{ eV}$ . The energy difference between  $s$  and  $p_x$  ( $p_y$ ) band to band transition decreases from  $32.6 \text{ meV}$  (XX) down to  $19.7 \text{ meV}$  (YY) with increasing  $h_{QD}$ .

$\mu$ -PL measurements of QDs of different nominal thicknesses exhibit high optical quality with sharp excitonic peaks. In order to get a meaningful identification of these spectra, we have calculated the few-particle binding energies. We have shown that the direct Coulomb interactions are insufficient to reproduce the experimental findings and that the inclusion of correlation effects allows the positive binding energy of the negatively charged exciton and of the biexciton to be explained. Binding states of the different excitonic complexes have been shown to be in reasonable agreement with experimental observations. For the thickest QDs, an improved agreement is expected by including  $d$  and higher excited states in the evaluation of the correlation effects. Our model of the anisotropic QD shape leads to a calculated FSS ranging from  $16$  to  $36 \mu\text{eV}$ , as the dot height decreases from  $7.5 \text{ nm}$  to  $3.3 \text{ nm}$ . The trend of increasing FSS with decreasing QD height is in qualitative agreement with experimental observations; however the calculated FSS underestimates the experimental values. The discrepancy between calculation and FSS increases as the QD height decreases, which is likely due to the fact that our model considers a  $C_{2v}$  symmetry which is lost in the smallest QDs due to higher degree of asymmetry at the bottom of the nanohole. Further studies, out of the scope the present work, should extend the model to  $C_s$  symmetry QDs.

- 
- [1] M. V. Durnev, M. Vidal, L. Bouet, T. Amand, M. M. Glazov, E. L. Ivchenko, P. Zhou, G. Wang, T. Mano and N. Ha, *Phys. Rev. B* **93**, 245412 (2016).
- [2] M. V. Durnev, M. M. Glazov, E. L. Ivchenko, M. Jo, T. Mano, T. Kuroda, K. Sakod, S. Kunz, G. Sallen, L. Bouet, X. Marie, D. Lagarde, T. Amand, and B. Urbaszek, *Phys. Rev. B* **87**, 085315 (2013).
- [3] G. Sallen, B. Urbaszek, M. M. Glazov, E. L. Ivchenko, T. Kuroda, T. Mano, S. Kunz, M. Abbarchi, K. Sakoda, D. Lagarde, A. Balocchi, X. Marie, and T. Amand, *Phys. Rev. Lett* **107**, 166604 (2011).
- [4] A. Nemcsics, Ch. Heyn, L. Toth, L. Dobos, A. Stemmann, W. Hansen, *J. Cryst. Growth* **335**, 58 (2011).
- [5] Ch. Heyn, M. Klingbeil, Ch. Strelow, A. Stemmann, S. Mendach, and W. Hansen, *Nanoscale Res. Lett.* **5**, 1633 (2010).
- [6] A. Graf, D. Sonnenberg, V. Paulava, A. Schliwa, Ch. Heyn, and W. Hansen, *Phys. Rev. B.* **89**, 115314 (2014).
- [7] P. Atkinson, E. Zallo, and O. G. Schmidt, *J. Appl. Phys.* **112**, 054303 (2012).
- [8] Ch. Heyn, A. Stemmann, T. Köppen, Ch. Strelow, T. Kipp, M. Grave, S. Mendach, and W. Hansen, *Appl. Phys. Lett.* **94**, 183113 (2009).
- [9] Y. H. Huo, A. Rastelli, and O. G. Schmidt, *Appl. Phys. Lett.* **102**, 152105 (2013).
- [10] Y. H. Huo, V. Křápek, A. Rastelli, and O. G. Schmidt, *Phys. Rev. B.* **90**, 041304(R) (2014).
- [11] Ch. Heyn, A. Küster, A. Ungeheuer, A. Gräfenstein, and W. Hansen, *Phys. Rev. B* **96**, 085408 (2017).
- [12] N. N. Ledentsov, *Semicond. Sci. Technol.* **26**, 014001 (2011).
- [13] D. Zhou, G. Sharma, S. F. Thomassen, T. W. Reenaas, and B. O. Fimland, *Appl. Phys. Lett.* **96**, 061913 (2010).
- [14] M. Zielinski, Y. Don, and D. Gershoni, *Phys. Rev. B* **91**, 085403 (2015).
- [15] Z. Trabelsi, M. Yahyaoui, K. Boujdaria, M. Chamarro, and C. Testelin, *J. Appl. Phys.* **121**, 245702 (2017).
- [16] P. Aonso-Gonzalez, B. Alén, D. Fuster, Y. Gonzalez, and L. Gonzalez, *Appl. Phys. Lett.* **91**, 163104 (2007).

- [17] L. Wang, V. Krapek, F. Ding, F. Horton, A. Schliwa, D. Bimberg, A. Rastelli, and O. G. Schmidt, Phys. Rev. B. **80**, 085309 (2009).
- [18] D. Sonnenberg, A. Graf, V. Paulava, W. Hansen, and C. Heyn, Appl. Phys. Lett. **101**, 143106 (2012).
- [19] B. J. BenDaniel and C. B. Duke, Phys. Rev. **152**, 683 (1966).
- [20] I. Saïdi, S. Ben Radhia, and K. Boujdaria, J. Appl. Phys. **107**, 043701 (2010).
- [21] Lelong P 1997 *PhD Thesis* Université Pierre et Marie Curie, Paris 6.
- [22] I. Saïdi, K. Sellami, M. Yahyaoui, C. Testelin, and K. Boujdaria, J. Appl. Phys. **109**, 033703 (2011).
- [23] M. Yahyaoui, K. Sellami, S. Ben Radhia, K. Boujdaria, M. Chamarro, B. Eble, C. Testelin, and A. Lemaître, Semicond. Sci. Technol. **29**, 075013 (2014).
- [24] For all the eigenstates  $(s, p_x, p_y)$  and both carriers (electron, hole), the Gaussian fits reproduced with a high accuracy the WF density.
- [25] M. Grundmann, O. Stier, D. Bimberg, Phys. Rev. B. **52**, 11969 (1995).
- [26] W. J. Moore and R. T. Holm, J. Appl. Phys. **80**, 6939 (1996).
- [27] A. Schliwa, M. Winkelnkemper, D. Bimberg, Phys. Rev. B. **79**, 075443 (2009).
- [28] M. Gong, W. Zhang, G. C. Guo, L. He, Appl. Phys. Lett. **99**, 231106 (2011).
- [29] P. Lelong and G. Bastard, Solid State Commun. **98**, 819 (1996).
- [30] H. Tong and M.W. Wu, Phys. Rev. B **83**, 235323 (2011).
- [31] J. D. Plumhof, V. Křápek, L. Wang, A. Schliwa, D. Bimberg, A. Rastelli, and O. G. Schmidt, Phys. Rev. B **81**, 121309 (2010).